IOP Publishing Journal of Physics B: Atomic, Molecular and Optical Physics
J. Phys. B: At. Mol. Opt. Phys. **57** (2024) 215603 (11pp) https://doi.org/10.1088/1361-6455/ad7e8a

The influence of resonant light pulses on high harmonic generation in solids

Tian-Jiao Shao*, Fang Hu*, Qiu-Lan Zhang, Huan-Qing Zou and Ai-Guo Yang

School of Information Science and Engineering, NingboTech University, Ningbo 315100, People's Republic of China

E-mail: shaotj@nit.zju.edu.cn and hufang@nit.net.cn

Received 29 June 2024, revised 5 September 2024
Accepted for publication 23 September 2024
Published 4 October 2024

Abstract

We have theoretically studied high harmonic generation (HHG) in solids driven simultaneously by a mid-infrared (MIR) laser and a high-order harmonic pulse with energy around the band gap between the valence band and conduction band. By adding this resonant harmonic light pulse with the relative intensity ratio of 4%, the high-order harmonic emission from the crystal is enhanced by 1–2 orders of magnitude. The yield of HHG in solid increases monotonically with the relative strength of the resonant harmonic pulses. In addition, we also found that HHG dynamics from the k channel around the boundary of the Brillouin zone can be selectively enhanced by adjusting the frequency of the resonant high-order harmonic pulse. The resonance-enhanced HHG and k channel selection effect in solids is also investigated by using the three-band semi-conductor Bloch equation for HHG in ZnO. We also find that the harmonic in the plateau region driven by adding a resonant light field to the strong MIR driving field has less red-shifted compared with the case driven by the MIR driving field alone.

Keywords: high-order harmonic generation, resonance, channel selection

1. Introduction

High harmonic generation (HHG) [1] is of great significance for generating ultrafast attosecond light sources [2, 3], developing x-ray light sources in the water window and imaging atoms and molecules at attosecond time scale and sub-nanometer spatial scale [4–7]. HHG in gas medium has been extensively studied. Based on the semi-classical three-step re-collision model [8], the strong field approximation model [9], and the time-dependent Schrödinger equation (TDSE) [10], theoretical complete solutions for HHG in gas have been developed.

Due to the development of the midinfrared (MIR) and terahertz laser technology [11, 12], a series of experimental [13–34] and theoretical [35–58] studies have verified that femtosecond lasers interacting with solids can also produce HHG, and HHG in solid have become a hot research topic. In the past, strong-field experiments in solids were limited by the material damage threshold and the absorption effect of high-energy photons by the solid medium [30]. The MIR and terahertz light sources have lower single photon energy, which means that transitions need to absorb a greater number of photons and high-order nonlinear processes have smaller optical absorption cross-sections. Therefore, for the same solid medium, lasers with longer wavelengths have correspondingly higher damage thresholds.

Using MIR and terahertz lasers as driving light, experiments have been reported on zinc oxide (ZnO) [13, 21, 34], magnesium oxide (MgO) [22], molybdenum disulfide [33], crystalline silicon [24], gallium selenide (GaSe) [15, 19], graphene [26] and other materials. HHG in wide bandgap semiconductors such as argon crystal and krypton crystal [17], quartz (α-SiO_2) [14, 28], amorphous fused quartz [23], and sapphire (Al_2O_3) [18, 31] were investigated. Because of the larger band gap and higher breakdown threshold,

* Authors to whom any correspondence should be addressed.

these materials are driven by near-infrared lasers to generate harmonic radiation and high-energy harmonic photons of about 40 electron volts are observed.

Compared with atomic and molecular systems, the dense atomic density and very ordered atomic arrangement in solids make HHG in solids a promising candidate for the development of compact and solid attosecond light sources. HHG in solid exhibits many characteristics that are different from its counterpart in gas medium such as the linear dependence of the cut-off energy of HHG on the peak field strength of the driving laser [13, 35, 36], multi-plateau structure [17, 20], unique dependence on the ellipticity of the driving field [13, 26, 44, 46, 50], the crystal orientation angle [19, 22], the wavelength of driving field [21], the polarization [13, 25], and so forth.

The electrons initially in the valence bands (VBs) are excited to the conduction bands driven by the laser, and then the electrons and holes move along the energy bands driven by the laser field and accumulate phases. The electrons and holes recombine and harmonic photons are emitted which carry the information of the energy band. Therefore, HHG in solids has ultrafast time resolution and provides an all-optical measurement to detect the electronic band structure of the material [16, 42], Berry curvature [28], probing the lattice dynamics [29], and electronic structure information such as transition dipole moment [49] and valence electron density distribution [32].

A series of recent works have explored HHG in solids controlled by light fields. In 2009, Calegari *et al* generated an HHG continuum with energy exceeding 200 eV efficiently in the experiment by an intense two-color field composed of 800 nm pulse and 1.45 μm IR pulse in Ne gas medium [59]. In 2015, Schütte *et al* investigated experimentally two-color HHG in a high-pressure Ne gas cell and observed an extreme-ultraviolet continuum extends to 160 eV which supports a bright isolated attosecond pulse [60]. In 2017, Saito *et al* used a circularly polarized laser as the driving pulse, and the HHG in solid shows a transition selection rule corresponding to the point group of the crystal material [27]. Only harmonics that satisfy the transition selection rules will have signals. Li *et al* investigated HHG in solid driven by the two-color field and found that the intensity of the second plateau can be enhanced in an appropriate two-color field compared to the results in a single-color field while maintaining the same amplitude [61]. Bruner *et al* found the HHG photon flux can be significantly increased by 1–2 orders of magnitude by using a bichromatic field [62]. Sun *et al* found that high harmonics in solids can be extended via resonant electron injection channels [63]. Tang and Bian explored the HHG in ZnO driven by an orthogonal two-color field [64].

The HHG driven by a two-color field composed of a fundamental laser field and a resonant harmonic was investigated in a gas medium. In 2003, HHG in He^+ driven simultaneously by a strong 800 nm laser and its 27th or 13th harmonic pulse was investigated [65]. Although the monochromatic 800 nm laser or its 27th harmonic pulse respectively ionize a low yield of He+, their combination resulted in a surprisingly high He^{2+} yield. The harmonic yield is enhanced by many orders of magnitude compared to the case of a fundamental pulse alone [65–67]. In this work, the influence of resonant harmonic pulses whose frequency is around the bandgap energy between the VB and conduction band on the HHG in solids is investigated by using the TDSE.

We found that light pulses with the energy around the bandgap cause a strong enhancement of the yield of HHG in solid. This is further confirmed by the crystal-momentum-resolved HHG spectra [48, 54]. It is found the harmonic yield increases monotonically with the relative intensity ratio of the resonant harmonic pulses. We also found that HHG from the k channel contributed by the k-point around the Brillouin zone (BZ) boundary can be selectively enhanced by adjusting the frequency of the resonant light pulse.

2. Results and discussion

The light–matter interaction is analyzed by the TDSE in the k-space [68] using the eigenstates obtained by using the Bloch states expansion method as described in previous works [37–39, 69]. The quasi-classical model used is discussed in the appendix. Unless not specifically noted, the calculations include initial crystal momentum in the entire BZ. The total HHG current is obtained by coherent summing of HHG current contributed by all initial crystal momentum k and then Fourier transform is performed to obtain the HHG yield at a given harmonic frequency [68]. The BZ is sampled with a uniform grid and the crystal momentum grid is fixed to be $\delta k \approx 0.079$ a.u. The evolution time grid is set as $\delta t \approx 0.377$ a.u.

The Mathieu-type potential is used and is given by,

$$V(x) = -V_0\left[1+\cos\left(2\pi x/a_0\right)\right], \tag{1}$$

where $V_0 = 0.37$ a.u. and lattice constant $a_0 = 8$ a.u. Figure 1(a) presents the calculated energy bands with the photon energy axis in harmonic order scale. The secondary horizontal axis with blue color in figure 1(a) is with eVs as energy scale.

The VB, conduction band 1 (CB1), conduction band 2 (CB2), and conduction band 3 (CB3) are plotted by blue, red, orange, and purple lines, respectively. The minimum band gap between the VB and the CB1 is 4.18 eV. The lattice constant and band gap correspond to the wide band gap semiconductor like Zincblende AlN [38]. The Mathieu-type potential is simple compared to actual materials in experiments, while the systematic investigation by using this potential gives clues to look at HHG in solids irradiated simultaneously by the fundamental MIR laser and its resonant harmonic pulse.

The expression of the single-color fundamental laser field in this work can be expressed by,

$$E_f(t) = E_0 f(t)\cos\left(\omega_0 t+\phi\right), \tag{2}$$

where $f(t)$ is the pulse envelope and ϕ is the relative phase between the fundamental laser and superposed harmonic pulse. To simulate the HHG processes in a real laser pulse, we use a cosine shape pulse envelope $f(t) = \cos\left(\pi\left(t-\tau/2\right)/\tau\right)$ which is shown by the blue dashed line in figure 2(a). ω_0 is the frequency of the laser field, E_0 is the peak field strength, τ is the duration of the temporal profile. If not differently

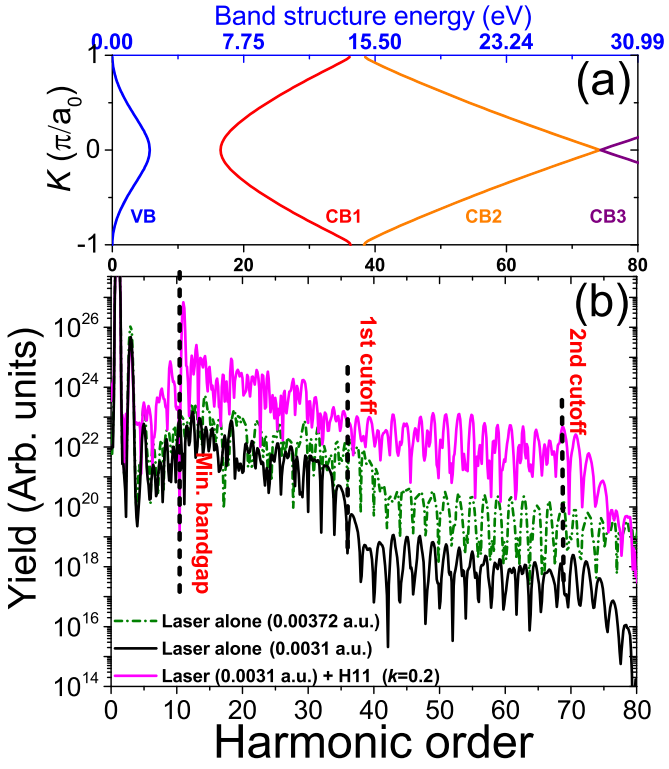

Figure 1. (a) The band structure of the periodical system was calculated by using the Bloch states expansion method. (b) The HHG spectra driven simultaneously by $E_0 = 0.0031$ a.u., 3200 nm laser and its 11th harmonic pulse with $\kappa = 0.2$ (magenta solid line), the case driven by $E_0 = 0.0031$ a.u., 3200 nm laser alone (black solid line), and the case driven by $E_0 = 0.003\,72$ a.u., 3200 nm laser alone (olive dashed line).

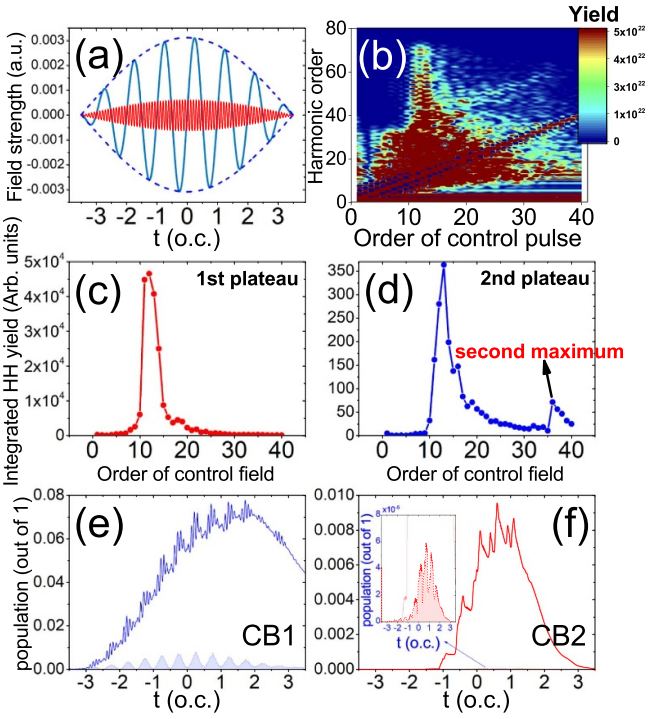

Figure 2. (a) The blue-solid line shows the temporal laser waveform of the fundamental $E_0 = 0.0031$ a.u. 3200 nm pulse. The blue-dashed line shows the temporal profile of the envelope. The red-solid line shows the temporal laser waveform of its 11th harmonics with relative strength ratio $\kappa = 0.2$. (b) HHG spectra driven simultaneously by the $E_0 = 0.0031$ a.u., 3200 nm laser field and its harmonic pulse with relative strength ratio $\kappa = 0.2$ as a function of the order of control harmonic field. (c) and (d) The integrated yields of the first plateaus (c) and the second plateaus (d) as a function of the order of the control harmonic field. (e) and (f) population of CB1 (e) and CB2 (f). Laser parameter: the fundamental pulse, 7 o.c., $E_0 = 0.0031$ a.u., 3200 nm pulse; the control pulse, its harmonic with relative strength ratio $\kappa = 0.2$.

specified, $E_0 = 0.0031$ a.u. (corresponding to laser intensity $I_0 = 3.373 \times 10^{11}\,\mathrm{W\,cm^{-2}}$), central wavelength $\lambda = 3200$ nm, and $\tau = 7$ optical cycle (o. c.) are used for the fundamental laser field in this work.

The superposed resonant harmonic pulse is given by,

$$E_h(t) = \kappa E_0 f(t) \cos(n\omega_0 t), \tag{3}$$

where κ is the relative strength ratio and n is the order of the superposed harmonic pulse. The two-color field by superposing the harmonic pulse field onto the fundamental laser can be expressed as,

$$E_{\mathrm{total}}(t) = E_f(t) + E_h(t). \tag{4}$$

2.1. Enhancement of the HHG yield in solids driven simultaneously by fundamental laser and its harmonic pulse

Figure 1(b) compares the HHG spectra driven by the $E_0 = 0.0031$ a.u., 3200 nm laser field alone (black solid line) and the case driven simultaneously by the $E_0 = 0.0031$ a.u. ($I_0 = 3.373 \times 10^{10}\,\mathrm{W\,cm^{-2}}$), 3200 nm laser field and its 11th harmonic pulse with relative strength ratio $\kappa = 0.2$ (corresponding to a relative intensity ratio of 4% and equal to $1.349 \times 10^{9}\,\mathrm{W\,cm^{-2}}$). Then the peak field strength of this two-color field is equal to 0.003 72 a.u. (corresponding to laser intensity $I_0 = 4.857 \times 10^{10}\,\mathrm{W\,cm^{-2}}$). For comparison, the HHG spectra driven by the $E_0 = 0.003\,72$ a.u., 3200 nm single-color laser field with the same total field strength is also plotted (olive dashed line).

The black dashed lines from left to right in figure 1(b) denote the minimum band gap between CB1 and VB, the band gap energy between CB1 and the VB at the boundary of the BZ which caused the cutoff energy of the first plateau, the cutoff energy of the second plateau, respectively.

The intensity of the first and second plateau (magenta solid line) is enhanced by nearly four orders in HHG driven simultaneously by the $E_0 = 0.0031$ a.u., 3200 nm laser and its 11th harmonic pulse with $\kappa = 0.2$ compared with the case of the $E_0 = 0.0031$ a.u., 3200 nm pulse alone (black solid line). It is two orders larger than the case driven by the $E_0 = 0.003\,72$ a.u., 3200 nm laser alone (olive dashed line).

In figure 2, we investigate the influence of the order of control harmonic pulse on the HHG yield. In figure 2(a), the temporal profile of the $E_0 = 0.0031$ a.u., 3200 nm laser and its 11th harmonic field with relative strength ratio $\kappa = 0.2$ are plotted by the blue solid line and red solid line, respectively.

Figure 2(b) presents the HHG spectra that vary with the order of the control harmonic field. By varying the order of the control harmonic pulse, around the 11th harmonic, the HHG spectra show a clear cut-off maximum. In figures 2(c) and (d), the red and blue scatters show the integrated yield of the 1st plateau and 2nd plateau of HHG spectra, respectively. The yield for 1st plateau and 2nd plateau is integrated with the spectral range from the 10.5th to 36th harmonic and from 36th to 75th, respectively. The red scatters in figure 2(c) indicate the enhancement of harmonic yield of 1st plateau when the order of control harmonic pulse is around $11\omega_0$ which corresponds to the minimum bandgap $E_g = 4.18$ eV ($10.8\omega_0$) between the VB and the CB1. In figure 2(d), the integrated yield of the 2nd plateau has two maximums, one is around the 11th harmonic and the other is around the 36th harmonic which corresponds to the minimum bandgap $E_g = 13.99$ eV ($36.1\omega_0$) between VB and CB2 at the boundary of the BZ. The case of other relative strength ratio of $\kappa = 0.1$ and $\kappa = 0.4$ are also calculated and can be found in appendix. We show the position of the maximums of the harmonic yield has little dependence on the relative strength of the auxiliary harmonic to fundamental MIR laser.

Figures 2(e) and (f) show the time-dependent population of CB1 and CB2 driven simultaneously by the $E_0 = 0.0031$ a.u., MIR laser field and its 11th harmonic pulse with relative strength ratio $\kappa = 0.2$, and the case driven by the $E_0 = 0.003\,72$ a.u., MIR laser alone. Under the same peak strength of the driving field, surprisingly, the population of CB1 is enhanced by nearly one order of magnitude due to the presence of the 11th harmonic pulse. The enhancement of the interband transition between VB and CB1 causes the first plateau of HHG spectra shown in figure 1(b) to be around two orders larger than the case driven by the $E_0 = 0.003\,72$ a.u., MIR laser field alone which has the same peak field strength. In figure 2(f), the increase in the population of CB2 explains why the intensity of the second plateau on HHG spectra is enhanced when the crystal is irradiated simultaneously by $E_0 = 0.0031$ a.u., MIR laser and its 11th harmonic pulse with relative strength ratio $\kappa = 0.2$. The inset shown in figure 2(f) indicates the population of CB2 is enhanced by more than two orders via resonant one-photon transitions.

Figure 3(a) schematically illustrates the resonant excitation at channel contributed by $k = 0$ (Γ point) driven simultaneously by 3200 nm laser field and its 11th harmonic pulse with energy corresponding to the minimum band gap between VB and CB1.

Figure 3(b) plots the energy of the emitted harmonic photons varying with the emission time by the quasi-classical model [40]. One can find by superposing an 11th harmonic pulse onto the fundamental $E_0 = 0.0031$ a.u., 3200 nm laser (magenta solid line), the energy of the HHG trajectories driven by the two-color field and the case of $E_0 = 0.0031$ a.u., 3200 nm single-color laser (black dashed-dotted line) are almost the same. The case of HHG trajectory driven by the $E_0 = 0.003\,72$ a.u., 3200 nm laser alone is also plotted for comparison (olive solid line).

Figures 3(c) and (d) present the time–frequency analysis of the HHG current driven by $E_0 = 0.003\,72$ a.u, 7 o.c., 3200 nm laser alone and the HHG driven simultaneously by the $E_0 =$

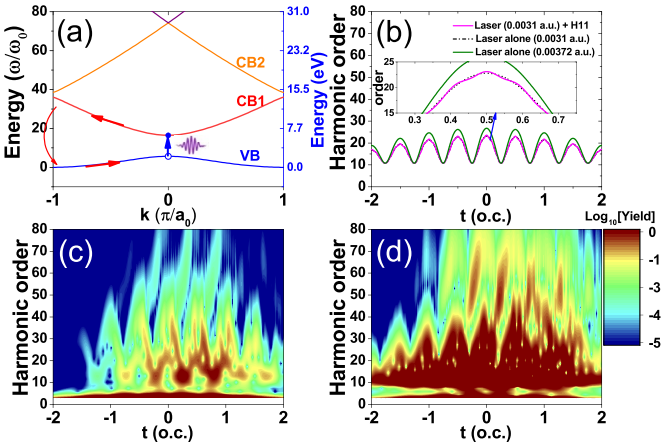

Figure 3. (a) Scheme plot of electron trajectory of HHG driven by laser field combined by $E_0 = 0.0031$ a.u., 3200 nm fundamental laser and its 11th harmonics with relative strength ratio $\kappa = 0.2$ in reciprocal space. (b) The energy of the emitted harmonic photons varies with the emission time by the quasi-classical model. (c) Temporal profile of HHG driven by $E_0 = 0.003\,72$ a.u., MIR pulse alone. (d) Temporal profile of HHG driven simultaneously by $E_0 = 0.0031$ a.u., MIR laser and its 11th harmonics with relative strength ratio $\kappa = 0.2$. The laser parameters in simulations are the same as the figure 2.

0.0031 a.u, 3200 nm laser field and its 11th harmonic pulse with relative strength ratio $\kappa = 0.2$, respectively. The time–frequency analysis is performed using the wavelet transform of the induced HHG current [70],

$$A_w(t_0,\omega) = \int d(t)\, w_{t_0,\omega}(t)\, \mathrm{d}t \equiv \mathrm{d}_\omega(t), \tag{5}$$

where $w_{t_0,\omega}(t) = \sqrt{\omega} W(\omega(t - t_0))$ is the wavelet kernel, ω is the frequency and $d(t)$ is the induced HHG current in the time domain. For the HHG emission, the Morlet wavelet is chosen as the mother wavelet.

$$W(x) = \left(1/\sqrt{\tau}\right) e^{ix} e^{-x^2/2\tau_{\mathrm{win}}^2} \tag{6}$$

where τ_{win} in the above equation is the window parameter of the wavelet transform. The dependence of $d_\omega(t)$ on the parameter τ_{win} has been tested by varying from 3 to 30. We choose $\tau_{\mathrm{win}} = 6$ to perform the wavelet transform which shows the best resolution in both the time and frequency domain.

The time–frequency analysis agrees with the population of conduction bands and shows the great enhancement of HHG yield due to the superposition of an 11th harmonic pulse.

2.2. The yield of HHG dependence on the relative strength of the resonant harmonic pulse

Figure 4 show the dependence of the integrated harmonic yield of the first plateau (blue scatters) and second plateau (black scatters) increase monotonously with the relative strength ratio of the control harmonic pulse. This can be explained by the population analysis in figures 2(e) and (f), due to the increase in the strength of the 11th harmonic pulse, the interband transition from VB to CB1 is enhanced and leads to the increase of HHG yield.

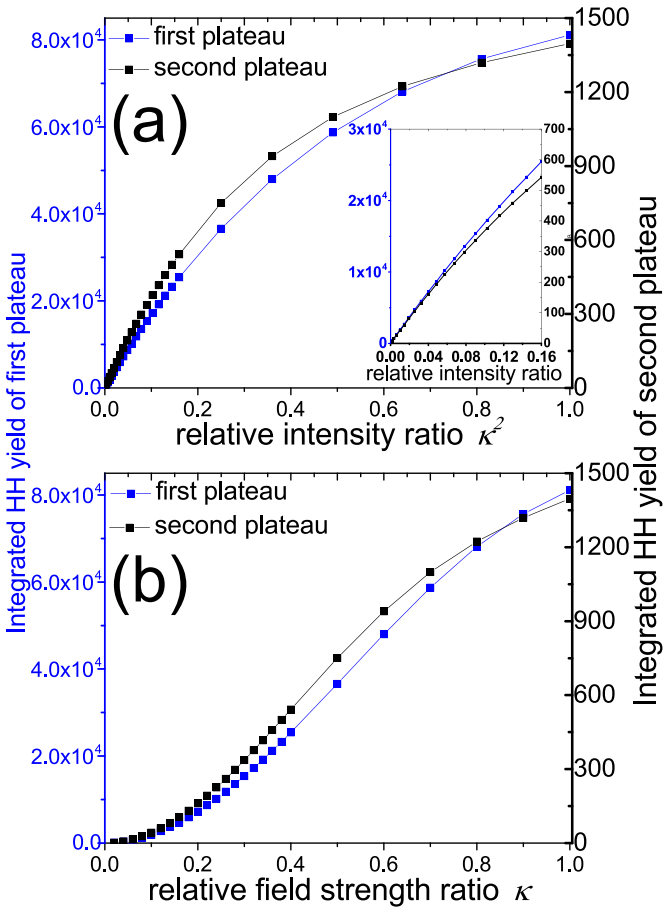

Figure 4. (a), (b) The integrated yield of the plateau region of HHG spectra vs the relative intensity ratio (a) and relative field strength ratio κ(b) of the 11th harmonic pulse, respectively. The integrated yield of the first plateau is integrated with the spectral range from the 12th to 36th harmonics. The integrated yield of the second plateau is integrated with the spectral range from 36th to 69th harmonics.

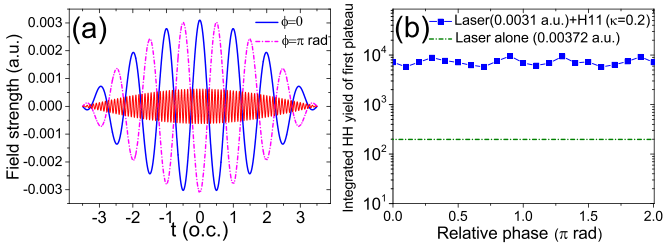

Figure 5. (a) Waveform representation of the MIR electric field for the relative two-color phase $\phi = 0$ and π rad, respectively. (b) The integrated yield of the first plateau region of HHG spectra as a function of the relative two-color phase ϕ. The two-color field is given by $E(t) = E_0 f(t)[\cos(\omega_0 t + \phi) + \kappa E_0 \cos(n\omega_0 t)]$.

As shown in figure 4(a), it can be seen that the yield of harmonics increases rapidly with the relative intensity ratio at the beginning. However, this dependence on the relative intensity ratio gradually slows down later on. Generally speaking, the ratio between the amplitudes of the fundamental pulse and its high harmonic pulse cannot be very large, due to the relatively low efficiency of the HHG process.

Figure 4(b) presents the dependence of integrated HHG yield on the relative strength ratio κ. Initially, the integrated HHG yield increases slowly with the relative strength ratio. And then, around $\kappa = 0.2$, the increase of HHG yield with relative strength ratio becomes rapid. As the relative strength ratio κ continued to increase, the increase of HHG yield with the κ began to slow down again.

The influence of the relative phase between the fundamental MIR field and control harmonic pulse is presented in figure 5. Figure 5(a) presents the MIR electric field for the case of two relative two-color phases $\phi = 0$ and π rad, respectively. Figure 5(b) shows that the harmonic yield is indeed dependent on the relative phase between the MIR laser and resonant harmonic pulses. However, in any relative phase situation, the resonance harmonic pulse-enhanced HHG yield is nearly two orders of magnitude higher than that of HHG driven by a single-color laser with the same field strength.

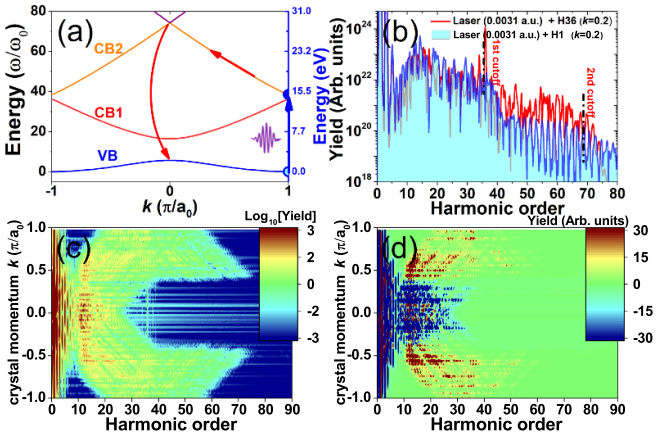

Figure 6. (a) Scheme plot of electron trajectory of HHG driven by laser field combined by $E_0 = 0.0031$ a.u., 3200 nm laser and its 36th harmonics with relative strength ratio $\kappa = 0.2$ in reciprocal space. (b) Comparison of the HHG spectra driven simultaneously by the $E_0 = 0.0031$ a.u., 3200 nm laser field and its 36th harmonic pulse with the case driven by the $E_0 = 0.003\,72$ a.u., 3200 nm laser field alone. (c) The crystal-momentum-resolved HHG spectra are driven simultaneously by the $E_0 = 0.0031$ a.u., 3200 nm laser field and its 36th harmonic pulse with relative strength ratio $\kappa = 0.2$. (d) The HHG yield difference obtained by subtracting the yield of the HHG spectra driven simultaneously by $E_0 = 0.0031$ a.u., 3200 nm laser field and its 36th harmonic pulse with relative strength ratio $\kappa = 0.2$ to the case driven by the $E_0 = 0.003\,72$ a.u. 3200 nm laser field alone. The HHG yield difference is plotted on a linear scale. Laser parameter: the single-color field: 7 o.c. (duration), 3200 nm, $E_0 = 0.003\,72$ a.u.; the two-color field: the fundamental pulse, 7 o.c., 3200 nm pulse, $E_0 = 0.0031$ a.u.; the control pulse, its 36th harmonic with relative strength ratio $\kappa = 0.2$.

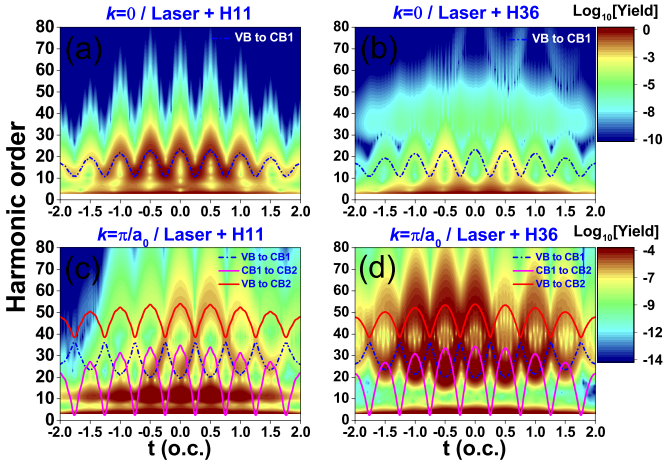

Figure 7. The time–frequency analysis of the HHG current contributed by single k channel plotted on a logarithmic scale. Left column: the time–frequency analysis of the HHG current generated by the $E_0 = 0.0031$, 3200 nm laser and its 11th harmonic pulse ($\kappa = 0.2$). Right column: the time–frequency analysis of the HHG current generated by the $E_0 = 0.0031$, 3200 nm laser and its 36th harmonic pulse ($\kappa = 0.2$). (a) and (b) Contributions from the k channel at $k = 0$ (Γ point). (c) and (d) Contributions from the k channel at $k = \pi/a_0$. The solid and dashed curves represent the energy of emitted harmonic photons by the quasi-classical model.

2.3. k channel selection by the resonant harmonic pulse

Figure 6(a) schematically shows an electron initially located at $k = \pi/a_0 = 0.3927$ a.u. in the VB, where excitation directly to the $k = \pi/a_0$ in the CB2 occurs due to the irradiation by the fundamental 3200 nm laser and 36th harmonic pulse simultaneously. Figure 6(b) compare the HHG spectra driven simultaneously by the fundamental 3200 nm laser and 36th harmonic pulse (red solid line) and the case driven by $E_0 = 0.003\,72$ a.u. laser alone (blue solid line). The second plateau of HHG spectra is enhanced by more than one order compared with the case driven by the MIR laser alone. Figure 6(c) shows the crystal-momentum-resolved HHG spectra driven simultaneously by the $E_0 = 0.0031$ a.u., 3200 nm laser and its 36th harmonic pulse with $\kappa = 0.2$. Figure 6(d) shows the HHG yield difference obtained by subtracting the yield of the case driven simultaneously by the MIR laser and its 36th harmonic with relative strength ratio $\kappa = 0.2$ to the case driven by the MIR laser alone. The darkest red indicates the HHG contributed by k channel at $k = \pi/a_0$ is strengthened.

Figures 7(a)–(d) show the time–frequency analysis of the HHG current contributed by the k channel at $k = 0$ (left column) and $k = \pi/a_0$ (right column), respectively. The comparison of figures 7(a) and (b) show the time–frequency analysis of the HHG current and the emission is enhanced at $k = 0$ by superposing an 11th harmonic pulse with the energy around the bandgap between VB and CB1 at $k = 0$. However,

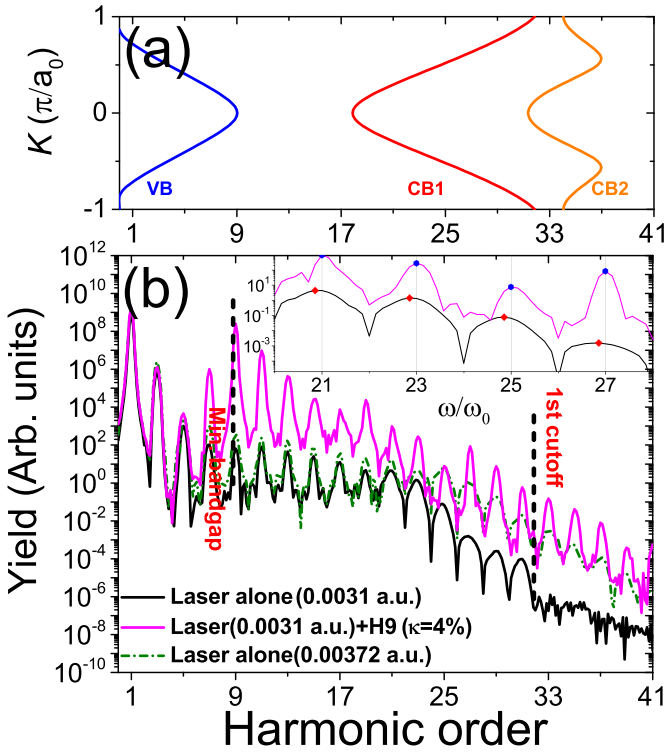

Figure 8. (a) The band structure of the wurtzite ZnO along the high symmetry direction Γ-M calculated by using the DFT. (b) The HHG spectra driven simultaneously by $E_0 = 0.0031$ a.u., 3500 nm laser and its 9th harmonic pulse with $\kappa = 0.2$ (red dashed line), the case driven by $E_0 = 0.0031$ a.u., 3500 nm laser alone (black solid line), and the case driven by $E_0 = 0.003\,72$ a.u., 3500 nm laser alone (blue dashed line).

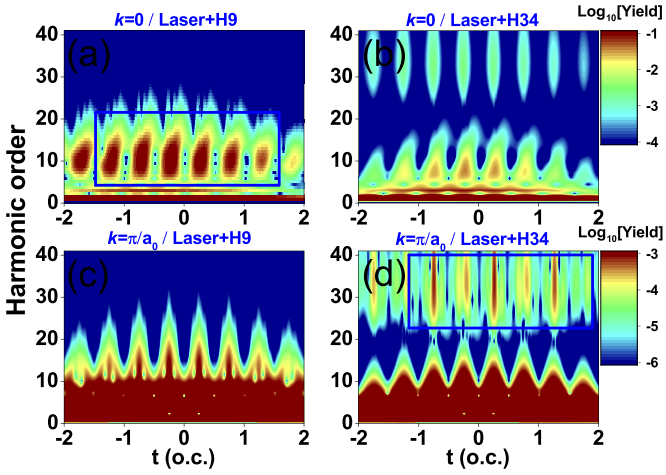

Figure 9. The time–frequency analysis of the HHG current in ZnO contributed by a single k channel plotted on a logarithmic scale. Left column: the time–frequency analysis of the HHG current generated by the $E_0 = 0.0031$, 3500 nm laser and its 9th harmonic pulse ($\kappa = 0.2$). Right column: the time–frequency analysis of the HHG current generated by the $E_0 = 0.0031$, 3500 nm laser and its 34th harmonic pulse ($\kappa = 0.2$). (a) and (b) Contributions from the k channel at $k = 0$ (Γ point). (c) and (d) Contributions from the k channel at $k = \pi/a_0$. The energy of the 9th harmonic corresponds to the minimum band gap between VB and CB1 at $k = 0$, and the energy of the 34th harmonic corresponds to the band gap between VB and CB2 at $k = \pi/a_0$. The blue solid rectangular marks the enhanced k channel of HHG emission in the time domain.

for the case driven by $E_0 = 0.0031$ a.u., 3200 nm laser field, and its 36th harmonic pulse with relative strength ratio $\kappa = 0.2$, the time–frequency analysis of the HHG current contributed by the k channel at $k = \pi/a_0$ is enhanced instead. The time–frequency analysis of the HHG contributed by the k channel from $k = 0$ and $k = \pi/a_0$ is in agreement with the crystal-momentum-resolved HHG spectra shown in figure 6.

2.4. Resonant high order harmonic pulse enhanced HHG in ZnO

In the following, we use the three-band semi-conductor Bloch equation to simulate the HHG in ZnO driven simultaneously by the fundamental 3500 nm laser pulse and its high order harmonic pulse [71], the dephasing time $T_2 = 2$ fs. As shown in figure 8, due to the addition of resonant light pulses, the harmonic yield of HHG in ZnO is increased by 1 to 2 orders of magnitude. The enhancement of HHG yield via resonant one-photon transitions is much more efficient than the case of increasing the field strength of driving the laser directly. Figure 8(a) shows the band structure of the wurtzite ZnO along the high symmetry direction Γ-M.

In figure 8(b), another feature is that the spectrum from ZnO driven by the MIR pulse alone is red-shifted, which is marked by the red scatters for clarity. This is because the harmonics are mainly generated after the peak of the MIR driving field and the intensity gradient decrease in the trailing edge leads to the red-shift of harmonic [31, 41]. By overlying with resonant fields, the transitions from the VB to the CB are enhanced via resonant one-photon transitions in earlier cycles. The HHG contribution from the leading edge increases and its blue-shift feature compensates for the red-shift in the trailing edge. Therefore, from the inset shown in 8(b), the frequency shift almost disappears.

Figure 9 shows the time–frequency analysis of the HHG current in ZnO contributed by the k channel at $k = 0$ (left column) and $k = \pi/a_0$ (right column), respectively. The comparison of figures 9(a) and (b) show the time–frequency analysis of the HHG current is enhanced at $k = 0$ by superposing a 9th harmonic pulse with the energy around the bandgap between VB and CB1 at $k = 0$. However, by comparing figures 9(c) and (d), for the case driven by $E_0 = 0.0031$ a.u., 3500 nm laser field, and its 34th harmonic pulse, the time–frequency analysis of the HHG current contributed by the k channel at $k = \pi/a_0$ is enhanced instead. In ZnO, the appeared condition is similar as the result from model simulation by using TDSE.

In addition, we investigate the role of resonant harmonic pulse in opening quantum paths in the HHG in ZnO. By shaping the laser field, the quantum path can be selectively enhanced and suppressed [72–74]. By further adding the resonant harmonic, the originally suppressed quantum path can be opened. The detailed results can be found in appendix B.

3. Conclusion

In conclusion, our research shows that under the fundamental 3200 nm laser and its high-order harmonic pulse, the excitation rate of the conduction band increases. The strengthening of the interband transition causes the yield of the HHG spectra enhanced by nearly two orders compared with the case driven by the MIR laser alone with the same peak field strength. With the increase of the relative strength of the control harmonic pulse, the yield of HHG spectra increases monotonously.

Specially, the 11th and 36th harmonics are considered in this work. The 11th harmonic with the energy around the minimum gap between VB and CB1 resonantly excited the electron from the k channel at $k = 0$ at VB to $k = 0$ at CB1. While the 36th harmonics with the energy around the minimum bandgap between VB and CB2 resonantly excited the electron from the $k = \pi/a_0$ at VB to $k = \pi/a_0$ at CB2. The k channel contributed by the k-points around the boundary of the BZ can be selectively enhanced by using the 36th harmonic.

The resonance-enhanced HHG and k channel selection effect in solids is also investigated by using the three-band semi-conductor Bloch equation for HHG in ZnO which accords with the result from model potential by using TDSE. Additionally, it is found that the harmonic in the plateau region driven by superposing a resonant light field to the strong MIR driving field has less red-shifted compared with the case driven by the MIR driving field alone. We also show quantum paths in HHG can be selectively opened by the addition of resonant harmonic.

This work provides insights into the physics of resonance-enhanced HHG in solids and is promising to be used to enhance the brightness of ultrafast extreme violet light sources.

Data availability statement

All data that support the findings of this study are included within the article (and any supplementary files).

Acknowledgments

We thank the support from the National Natural Science Foundation of China (No. 12104395), Zhejiang Provincial Natural Science Foundation of China (No. LQ22A040004), and the Ningbo Natural Science Foundation (Nos. 2021J153 and 2023J289). The authors thank the referees for their helpful comments.

Appendix A. First-principles calculations

The band structures of the wurtzite ZnO (w-ZnO) used in our work were performed by using the projector augmented wave method, implemented by the Vienna *ab initio* simulation package (VASP) [75]. The local-density approximation (LDA) is used for exchange-correlation functional.

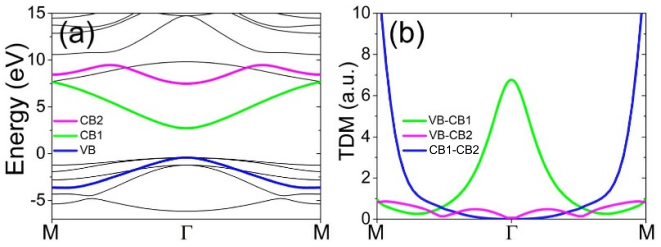

Figure A1. (a) Band dispersion along the Γ-M and (b) transition dipole moment between the valence band and conduction band along the Γ-M of wurtzite ZnO.

Since the Zn atoms have partially filled d orbitals. The common LDA approximation fails to treat the strong mutual interactions between the d orbitals. LDA + U method is proposed to correct the self-interaction empirically [76, 77]. The LDA + U method is employed in DFT calculation for ZnO in this work. A plane-wave cutoff of 500 eV was adopted. The k-points were set to $18 \times 18 \times 12$ for sampling the BZ of the w-ZnO unit cell with Monkhorst-Pack method.

After geometry optimization calculation, the optimized lattice constant parameters for w-ZnO are $a = 2.969$ Å and $c = 4.784$ Å, respectively. This is consistent with the experimental reported $a = 3.24$ Å and $c = 5.19$ Å. The calculation shows a minimum band gap value of 3.133 eV which accords with the experimentally measured 3.30 eV [78]. The transition dipole is obtained by the process of DFT result by using the post-processing program VASPKIT [79]. When driven by a linear polarized laser field, the VB (red), CB1 (blue), and CB2 in figure A1(a) contribute predominantly to the HHG spectra. Figure A1(b) shows the transition dipole moment (TDM) between the VB, CB1, and CB2. In the three-band SBE calculation, the energy band structures and TDM calculated by DFT are expanded by the Fourier series.

Appendix B. Opening quantum path by the auxiliary control harmonic pulse in ZnO

In this part, we show the quantum path in HHG process can be opened by the auxiliary resonant harmonic pulse. The ω-2ω two-color field is defined as,

$$E(t) = E_0 f(t) \left[\cos(\omega_0 t) + \kappa_s \cos(2\omega_0 t + \phi_s)\right], \qquad \text{(B.1)}$$

where $E_0 = 0.0019$ a.u. is the amplitude of the fundamental laser field, ω_0 is the angular frequency of the fundamental 3500 nm laser field with a full width of half maximum (FWHM) of 150 fs. $\kappa_s = 0.1$ is the relative field strength of the second harmonic. $\phi_s = \pi$ rad is the relative phase of the second harmonic. Shown in figure B1(a) are the electric fields of the

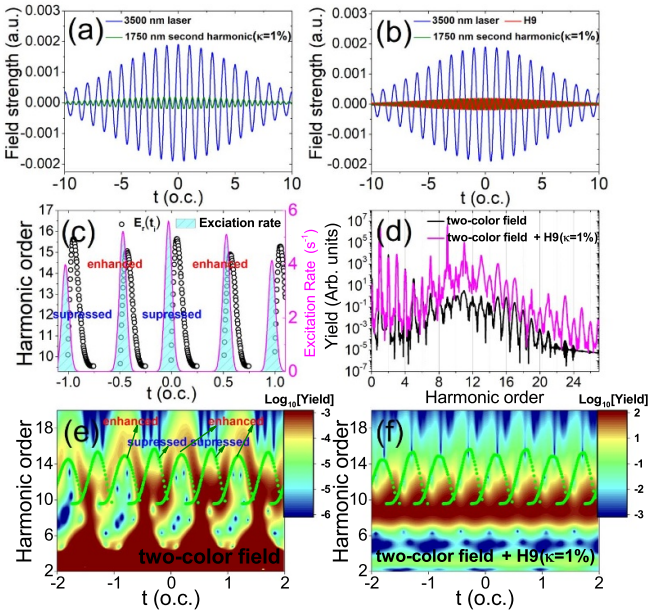

Figure B1. (a) and (b) Waveform representation of the electric field for ω-2ω two-color field (a) and the two-color field superposed by its 9th harmonic pulse (b). (c) The harmonic photon energy varies as a function of the ionization time (black circles). The magenta solid line represents the time-dependent excitation rates. (d) Comparison of the HH spectra driven by the ω-2ω two-color field and ω-2ω two-color field superposed by a resonant 9th harmonic pulse. (e) and (f) The time–frequency analysis of the HHG current driven by the ω-2ω two-color field (e) and ω-2ω two-color field superposed by a resonant 9th harmonic pulse (f), respectively. The green scatters shows harmonic photon energy as a function of recombination time of electron/hole pairs predicted by the semi-classical analysis [36].

fundamental 3500 nm laser and its second harmonic with a relative phase of π rad (a time delay equal to 0.25 o.c. of 3500 nm laser).

Figure B1(c) presents the harmonic photon energy (black circles) plotted as a function of ionization time [36] and the time-dependent excitation rate (gray-filled curve) calculated by the Keldysh model. We can see the electrons excited around $t = -0.5$ o.c. and $t = 0.5$ o.c. will return with high energy and at the same time with a large excitation rate enabling the generated harmonic photon with an enhanced yield. Nevertheless, the electron trajectory excited around $t = -1.0$ o.c., $t = 0.0$ o.c., and $t = 1.0$ o.c. is observed with a low excitation rate which indicates the suppression of these quantum paths. This is further confirmed by performing the semi-conductor Bloch equation shown in figure B1(e). In figure B1(e), the green scatters represent the harmonic photon energy as a function of recombination time predicted by the semi-classical calculation [36]. In each optical cycle, there is only one HHG emission enhanced and one HHG emission is suppressed to near extinction.

Show in figure B1(b), are the three electric fields, including two-color ω-2ω laser field and the resonant 9th harmonic pulse,

$$E(t) = E_0 f(t)\left[\cos(\omega_0 t) + \kappa_s \cos(2\omega_0 t + \phi_s) + \kappa \cos(n\omega_0 t)\right], \tag{B.2}$$

where $\kappa_s = 0.2$ is the relative strength ratio of second harmonic, $\kappa = 0.1$ is the relative strength ratio of resonant harmonic pulse. By superposing this weak resonant harmonic pulse, the yield of HH spectra is increase by one to two orders. On the other hand, as shown in figure B1(d), for the two-color field, both even and odd harmonics have nearly the same yield due to the breaking of the temporal symmetry of the driving field. Nevertheless, the addition of the resonant harmonic pulse open the originally suppressed quantum path. As shown by the magenta solid line in figure B1(d), this weakens the even harmonic due to interference between neighboring half-cycle HHG processes. In figure B1(e), one can discover the originally suppressed quantum path is opened by adding the resonant harmonic pulse.

Appendix C. Quasi-classical model

In figures 3 and 7, the energy of emitted harmonic photons are predicted by the quasi-classical model. In this model, we suppose the electrons are initially at the Γ point ($k = 0$) before the laser arrives. This is because it is located at the eigenstate on top of VB1 in k-space which has the largest excitation rates according to the Keldysh model. The quasi-classical equation of the electrons can be expressed by [40],

$$k(t) = k_0 + \frac{e}{\hbar} A(t), \tag{C.1}$$

where k_0 is the initial wave vector at Γ point and $A(t)$ is the vector potential of the driving electric field. After interband transition by the driving field, the carrier does Bloch oscillation along the band driven by the driving electric field. When the electrons and holes recombine with each other, the harmonic photons are emitted with energy equal to the band energy difference between the two bands,

$$\eta(t) = \frac{\varepsilon_{b1}(k(t)) - \varepsilon_{b2}(k(t))}{\hbar\omega_0}, \tag{C.2}$$

where $\varepsilon_{b1}(k(t))$ and $\varepsilon_{b2}(k(t))$ are the energy of the band 1 and band 2, respectively. ω_0 is the angular frequency of the fundamental laser field.

Appendix D. Calculation for other relative strength of the auxiliary control harmonic pulse

Further, the effect of the relative strength ratio of the auxiliary control harmonic pulse on the HHG spectra is investigated. Figure D1 represents the HHG driven simultaneously by the $E_0 = 0.0031$ a.u., 3200 nm laser field and its harmonic pulse with relative strength ratio $\kappa = 0.1$ and $\kappa = 0.4$, respectively.

The result accords with the case of $\kappa = 0.2$ shown in figure 2 which indicates little dependence position of the peaks of the harmonic yield on the relative strength ratio of the auxiliary harmonic. The red scatters in figures D1(a) and (c) indicate the enhancement of harmonic yield of 1st plateau when the order of control harmonic pulse is around $11\omega_0$ which corresponds to the minimum bandgap $E_g = 4.18$ eV ($10.8\omega_0$). While in figures D1(b) and (d), the integrated yield of the 2nd plateau

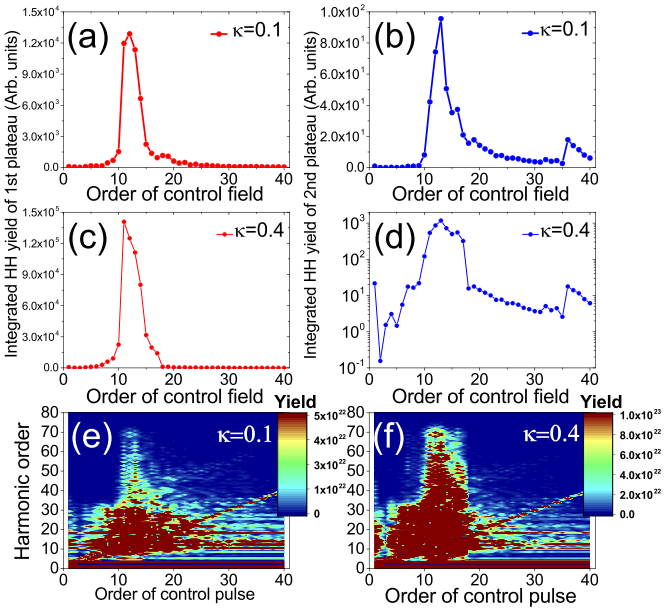

Figure D1. (a) and (b) The integrated yields of the first plateaus (a) and the second plateaus (b) as a function of the order of the control harmonic field for relative strength ratio $\kappa = 0.1$. (c) and (d) The integrated yields of the first plateaus (c) and the second plateaus (d) as a function of the order of the control harmonic field for relative strength ratio $\kappa = 0.4$. (e) and (f) HHG spectra driven simultaneously by the $E_0 = 0.0031$ a.u., 3200 nm laser field and its harmonic pulse with relative strength ratio $\kappa = 0.1$ (e) and $\kappa = 0.4$ (f) as a function of the order of control harmonic field, respectively.

has two maximums, one is around the 11th harmonic and the other is around the 36th harmonic corresponding to the minimum bandgap $E_g = 13.99$ eV ($36.1\omega_0$) between VB and CB2 at the boundary of the BZ. By varying the order of the control harmonic pulse, figures D1(e) and (f) show a clear cut-off maximum around the 11th harmonic.

ORCID iDs

Tian-Jiao Shao https://orcid.org/0000-0001-5178-4544
Qiu-Lan Zhang https://orcid.org/0000-0002-3153-3577

References

[1] McPherson A, Gibson G, Jara H, Johann U, Luk T S, McIntyre I, Boyer K and Rhodes C K 1987 *J. Opt. Soc. Am.* B **4** 595–601
[2] Paul P M, Toma E S, Breger P, Mullot G, Augé F, Balcou P, Muller H G and Agostini P 2001 *Science* **292** 1689–92
[3] Hentschel M, Kienberger R, Spielmann C, Reider G A, Milosevic N, Brabec T, Corkum P, Heinzmann U, Drescher M and Krausz F 2001 *Nature* **414** 509–13
[4] Lein M, Marangos J P and Knight P L 2002 *Phys. Rev.* A **66** 051404
[5] Itatani J, Levesque J, Zeidler D, Niikura H, Pépin H, Kieffer J C, Corkum P B and Villeneuve D M 2004 *Nature* **432** 867–71
[6] Bian X B and Bandrauk A D 2014 *Phys. Rev. Lett.* **113** 193901
[7] Ciappina M F *et al* 2017 *Rep. Prog. Phys.* **80** 054401
[8] Corkum P B 1993 *Phys. Rev. Lett.* **71** 1994
[9] Lewenstein M, Balcou P, Ivanov M Y, L'huillier A and Corkum P B 1994 *Phys. Rev.* A **49** 2117
[10] Feit M D, Fleck J A and Steiger A 1982 *J. Comput. Phys.* **47** 412–33
[11] Dubietis A, Jonušauskas G and Piskarskas A 1992 *Opt. Commun.* **88** 437–40
[12] Ishii N, Kaneshima K, Kitano K, Kanai T, Watanabe S and Itatani J 2014 *Nat. Commun.* **5** 3331
[13] Ghimire S, DiChiara A D, Sistrunk E, Agostini P, DiMauro L F and Reis D A 2011 *Nat. Phys.* **7** 138–41
[14] Luu T T, Garg M, Kruchinin S Y, Moulet A, Hassan M T and Goulielmakis E 2015 *Nature* **521** 498–502
[15] Hohenleutner M, Langer F, Schubert O, Knorr M, Huttner U, Koch S W, Kira M and Huber R 2015 *Nature* **523** 572–5
[16] Vampa G, Hammond T, Thiré N, Schmidt B, Légaré F, McDonald C, Brabec T, Klug D and Corkum P 2015 *Phys. Rev. Lett.* **115** 193603
[17] Ndabashimiye G, Ghimire S, Wu M, Browne D A, Schafer K J, Gaarde M B and Reis D A 2016 *Nature* **534** 520–3
[18] Han S, Kim H, Kim Y W, Kim Y J, Kim S, Park I Y and Kim S W 2016 *Nat. Commun.* **7** 13105
[19] Langer F *et al* 2016 *Nature* **533** 225–9
[20] You Y S *et al* 2017 *Opt. Lett.* **42** 1816–9
[21] Gholam-Mirzaei S, Beetar J and Chini M 2017 *Appl. Phys. Lett.* **110** 061101
[22] You Y S, Reis D A and Ghimire S 2017 *Nat. Phys.* **13** 345–9
[23] You Y S, Yin Y, Wu Y, Chew A, Ren X, Zhuang F, Gholam-Mirzaei S, Chini M, Chang Z and Ghimire S 2017 *Nat. Commun.* **8** 724
[24] Vampa G, Ghamsari B, Siadat Mousavi S, Hammond T, Olivieri A, Lisicka-Skrek E, Naumov A Y, Villeneuve D, Staudte A and Berini P 2017 *Nat. Phys.* **13** 659–62
[25] Liu H, Li Y, You Y S, Ghimire S, Heinz T F and Reis D A 2017 *Nat. Phys.* **13** 262–5
[26] Yoshikawa N, Tamaya T and Tanaka K 2017 *Science* **356** 736–8
[27] Saito N, Xia P, Lu F, Kanai T, Itatani J and Ishii N 2017 *Optica* **4** 1333–6
[28] Luu T T and Wörner H J 2018 *Nat. Commun.* **9** 916
[29] Zhang J, Wang Z, Lengers F, Wigger D, Reiter D E, Kuhn T, Wörner H J and Luu T T 2024 *Nat. Photon.* **18** 1–7
[30] Ghimire S and Reis D A 2019 *Nat. Phys.* **15** 10–16
[31] Kim Y W, Shao T J, Kim H, Han S, Kim S, Ciappina M, Bian X B and Kim S W 2019 *ACS Photonics* **6** 851–7
[32] Lakhotia H, Kim H, Zhan M, Hu S, Meng S and Goulielmakis E 2020 *Nature* **583** 55–59
[33] Lou Z, Zheng Y, Liu C, Zhang L, Ge X, Li Y, Wang J, Zeng Z, Li R and Xu Z 2020 *Opt. Commun.* **469** 125769
[34] Wang Y *et al* 2023 *Opt. Express* **31** 3379–89
[35] Vampa G, McDonald C R, Orlando G, Klug D D, Corkum P B and Brabec T 2014 *Phys. Rev. Lett.* **113** 073901
[36] Vampa G, McDonald C R, Orlando G, Corkum P B and Brabec T 2015 *Phys. Rev.* B **91** 064302
[37] Wu M, Ghimire S, Reis D A, Schafer K J and Gaarde M B 2015 *Phys. Rev.* A **91** 043839
[38] Hawkins P G, Ivanov M Y and Yakovlev V S 2015 *Phys. Rev.* A **91** 013405
[39] Guan Z, Zhou X X and Bian X B 2016 *Phys. Rev.* A **93** 033852
[40] Du T Y and Bian X B 2017 *Opt. Express* **25** 151–8
[41] Jia G R, Huang X H and Bian X B 2017 *Opt. Express* **25** 23654–62
[42] Lanin A, Stepanov E, Fedotov A and Zheltikov A 2017 *Optica* **4** 516–9
[43] Ikemachi T, Shinohara Y, Sato T, Yumoto J, Kuwata-Gonokami M and Ishikawa K L 2017 *Phys. Rev.* A **95** 043416
[44] Tancogne-Dejean N, Mücke O D, Kärtner F X and Rubio A 2017 *Nat. Commun.* **8** 745

[45] Jiang S, Chen J, Wei H, Yu C, Lu R and Lin C D 2018 *Phys. Rev. Lett.* **120** 253201
[46] Liu C, Zheng Y, Zeng Z and Li R 2018 *Phys. Rev.* A **97** 063412
[47] Li L, Lan P, Zhu X, Huang T, Zhang Q, Lein M and Lu P 2019 *Phys.Rev. Lett.* **122** 193901
[48] Navarrete F, Ciappina M F and Thumm U 2019 *Phys. Rev.* A **100** 033405
[49] Zhao Y T, yan Ma S, Jiang S C, Yang Y J, Zhao X and Chen J G 2019 *Opt. Express* **27** 34392–404
[50] Chen Z Y and Qin R 2019 *Opt. Express* **27** 3761–70
[51] Silva R E F, Martín F and Ivanov M 2019 *Phys. Rev.* B **100** 195201
[52] Li J, Zhang X, Fu S, Feng Y, Hu B and Du H 2019 *Phys. Rev.* A **100** 043404
[53] Zeng A W and Bian X B 2020 *Phys. Rev. Lett.* **124** 203901
[54] He Y L, Guo J, Gao F Y, Yang Z J, Zhang S Q and Liu X S 2021 *Phys. Rev.* A **104** 013104
[55] Wang X Q and Bian X B 2021 *Phys. Rev.* A **103** 053106
[56] Liu J Q and Bian X B 2021 *Phys. Rev. Lett.* **127** 213901
[57] Zuo R, Song X, Ben S, Meier T and Yang W 2023 *Phys. Rev. Res.* **5** L022040
[58] Chen J X and Bian X B 2024 *Phys. Rev.* A **109** 033104
[59] Calegari F, Vozzi C, Negro M, Sansone G, Frassetto F, Poletto L, Villoresi P, Nisoli M, Silvestri S D and Stagira S 2009 *Opt. Lett.* **34** 3125–7
[60] Schütte B, Weber P, Kovács K, Balogh E, Major B, Tosa V, Han S, Vrakking M J J, Varjú K and Rouzée A 2015 *Opt. Express* **23** 33947–55
[61] Li J B, Zhang X, Yue S J, Wu H M, Hu B T and Du H C 2017 *Opt. Express* **25** 18603–13
[62] Bruner B D, Narovlansky-Uzan A J, Arusi-Parpar T, Orenstein G, Shonfeld A and Dudovich N 2021 *J. Phys. B: At. Mol. Opt. Phys.* **54** 154001
[63] Sun N, Zhu X, Li L, Lan P and Lu P 2021 *Phys. Rev.* A **103** 053111
[64] Tang D and Bian X B 2021 *Phys. Rev.* B **104** 104302
[65] Ishikawa K 2003 *Phys. Rev. Lett.* **91** 043002
[66] Li P C, Zhou X X, Wang G L and Zhao Z X 2009 *Phys. Rev.* A **80** 053825
[67] Du H, Wang H and Hu B 2010 *Phys. Rev.* A **81** 063813
[68] Shao T J, Zhang Q L, Song Y D and Zou H Q 2023 *J. Phys. B: At. Mol. Opt. Phys.* **56** 165401
[69] Shao T J, Zou H Q and Zhang Q L 2022 *J. Phys. B: At. Mol. Opt. Phys.* **55** 235601
[70] Tong X M and Chu S I 2000 *Phys. Rev.* A **61** 021802
[71] McDonald C R, Vampa G, Corkum P B and Brabec T 2015 *Phys. Rev.* A **92** 033845
[72] Zeng Z, Cheng Y, Song X, Li R and Xu Z 2007 *Phys. Rev. Lett.* **98** 203901
[73] Song X, Zeng Z, Fu Y, Cai B, Li R, Cheng Y and Xu Z 2007 *Phys. Rev.* A **76** 043830
[74] Ishii N, Kosuge A, Hayashi T, Kanai T, Itatani J, Adachi S and Watanabe S 2008 *Opt. Express* **16** 20876–83
[75] Kresse G and Hafner J 1993 *Phys. Rev.* B **47** 558–61
[76] Perdew J P and Levy M 1983 *Phys. Rev. Lett.* **51** 1884–7
[77] Erhart P, Albe K and Klein A 2006 *Phys. Rev.* B **73** 205203
[78] Freeouf J L 1973 *Phys. Rev.* B **7** 3810–30
[79] Wang V, Xu N, Liu J C, Tang G and Geng W T 2021 *Comput. Phys. Commun.* **267** 108033

Web of Science™ Core Collection

经检索《Web of Science™ Core Collection》，下述论文被《SCI - Expanded》收录。（数据获取：2024年10月14日）

标题: The influence of resonant light pulses on high harmonic generation in solids

作者: Shao, TJ(Shao, Tianjiao) Hu, F(Hu, Fang) Zhang, QL(Zhang, Qiulan) Zou, HQ(Zou, Huanqing) Yang, AG(Yang, Aiguo)

来源出版物:JOURNAL OF PHYSICS B-ATOMIC MOLECULAR AND OPTICAL PHYSICS **卷:**57 **期:**21 **文献号:**215603

出版时间:2024,NOV 14 **DOI:**10.1088/1361-6455/ad7e8a

出版商:IOP Publishing Ltd **出版商地址:**TEMPLE CIRCUS, TEMPLE WAY, BRISTOL BS1 6BE, ENGLAND

文献类型: Article **语种:**English

入藏号:WOS:001326875400001 **IDS号:**H9W9E

地址:[Shao, Tian-Jiao; Hu, Fang; Zhang, Qiu-Lan; Zou, Huan-Qing; Yang, Ai-Guo] NingboTech Univ, Sch Informat Sci & Engn, Ningbo 315100, Peoples R China

通讯作者: Shao, TJ; Hu, F (通讯作者)，NingboTech Univ, Sch Informat Sci & Engn, Ningbo 315100, Peoples R China.

电子邮件:shaotj@nit.zju.edu.cn; hufang@nit.net.cn

ISSN:0953-4075 **电子ISSN:**1361-6455

ISO 来源文献缩写:J. Phys. B-At. Mol. Opt. Phys. **来源出版物页码计数:**11

注：

以上检索结果均得到被检索人的确认。本证明编号：NBT-SCIE-2024-11905

《SCI - Expanded》检索结果（收录情况）

浙大宁波理工学院图书馆

检索人(签名):

审核人(签章):

浙大宁波理工学院 图书馆 检索证明专用章

2024年12月16日

InCites™ Journal Citation Reports®

经检索《Web of Science™》的JCR数据库，期刊《JOURNAL OF PHYSICS B-ATOMIC MOLECULAR AND OPTICAL PHYSICS》2023年JCR的影响因子情况：

ISSN：0953-4075

eISSN：1361-6455

2023年影响因子：1.5

OPTICS：Q3

PHYSICS, ATOMIC, MOLECULAR & CHEMICAL：Q3

注：

1.以上检索结果均得到被检索人的确认。证明编号：NBT-SCIE-2024-11905-IF2023

2.论文的期刊影响因子应与该论文所发表期刊的年份相对应。

3.因JCR的最新数据截至到2023年，2024年出版论文的期刊影响因子以2023年的期刊影响因子为参考。

《JOURNAL CITATION REPORTS（JCR）》检索结果

浙大宁波理工学院图书馆

检索人(签名)：

审核人(签章)：

检索证明专用章

2024年12月16日